

# High-Cadence Observations of Magnetic Field Dynamics and Photospheric Emission Sources in the Eruptive Near-the-Limb X4.9 Solar Flare on 25 February, 2014: Evidences for Two-Stage Magnetic Reconnection during the Impulsive Phase

I. N. Sharykin<sup>a, \*</sup>, I. V. Zimovets<sup>a, b</sup>, and A. V. Radivon<sup>a, b</sup>

<sup>a</sup> *Space Research Institute, Russian Academy of Sciences (IKI), Moscow, Russia*

<sup>b</sup> *Moscow Institute of Physics and Technology (State University), Moscow, Russia*

\**e-mail: ivan.sharykin@phystech.edu*

Received April 13, 2023; revised April 17, 2023; accepted April 19, 2023

**Abstract**—We present an analysis of the pre-limb eruptive X4.9 solar flare on February 25, 2014, by means of which we confirm a hypothesis of the two-stage energy release corresponding to two magnetic reconnection regimes in the flare impulsive phase. This flare is selected, firstly, because of its morphological peculiarities suggesting the presence of the two energy release stages. Secondly, the flare was very suitably located near the solar limb and it was well-observed by many instruments. We performed an analysis of multiwavelength observational data of this flare region to find a connection between changes of the photospheric magnetic field, morphology of hard and soft X-ray sources, dynamics of the photospheric optical emission sources, metric radio bursts, and kinematics of an eruptive structure. The simultaneous usage of the line-of-sight and vector Helioseismic Magnetic Imager (HMI) magnetograms allowed us to trace magnetic field changes during the flare impulsive phase with high temporal resolution. HMI filtergrams allowed to trace displacement of the photospheric emission sources, associated with the magnetic reconnection, with very high temporal resolution up to 2 s. Using all observational results, we argue that the found flare stages are characterized by the following magnetic reconnection regimes. The first stage is predominantly characterized by the three-dimensional zipping reconnection in the strong sheared magnetic field assuming the tether-cutting geometry. The second stage corresponds to the so-called “standard” model of eruptive flares with the quasi-two-dimensional reconnection below the eruptive flux-rope. All observational peculiarities of these two stages are discussed in details.

DOI: 10.1134/S0010952523090010

## INTRODUCTION

Solar flares fall into two general classes: eruptive and confined flares [8, 31]. Eruptions can be small-scale (e.g. associated with localized jets and ejecta) or large-scale processes leading to coronal mass ejections (CMEs) with the energetics comparable with the energetics of other flare energy release channels, e.g. energies of thermal plasma and nonthermal particles [9]. Confined flares are usually assumed to be without a pronounced CME seen by coronagraphs. Investigation of these two flare classes is important for the fundamental solar physics as well as for the practical purpose in the context of the space weather forecasting. Indeed a clear understanding of differences between these two classes will help us to improve prediction models of interplanetary perturbations connected with CMEs.

Along with practical studies we need in more clear understanding of the eruptive processes and an

accompanied energy release during the flare impulsive phase accompanied by acceleration of particles, plasma heating and emission intensity growth in various spectral ranges [4]. There are a few basic questions, which still requires the answers. In particular, how does magnetic reconnection operate in time and 3D space, and how does magnetic field dynamics relate to magnetic reconnection and to different flare emissions observed during the impulsive phase and a developing eruption?

The “standard” 2D CSHKP model (SM—the standard model) of an eruptive two-ribbon solar flare [13, 24, 38, 44] assumes that a flare and eruption trigger is a “global” (e.g. kink or torus) MHD instability of a twisted magnetic flux rope. The erupting flux rope (a plasmoid in 2D) stretches overlying magnetic field lines (arch loops), and the 2D magnetic reconnection happens in a current sheet (with X-points) below the

erupting flux rope, which is a part of a developing CME. Despite of the relative simplicity of this model and success in explanation of some individual flares, it cannot be directly applied to many real (observed) situations. The thing is that magnetic field dynamics during the flare energy release is developed in a 3D space, rather than in a 2D space. At least, 2D models should be modified taking into account the 3rd dimension along the polarity inversion line (PIL) (let us call it 3DSM [2, 15, 16]). Today it is known that different 3D magnetic field topologies can be responsible for solar flares where the 3D magnetic reconnection of various types can be realized.

SM assumes interaction of opposite-polarity magnetic field lines at an X-point below an erupting flux rope. In a volume around the reconnection site, plasma is heated and thermal electrons are accelerated forming nonthermal populations with power-law (or more complicated) energy spectra [10, 47]. However, in a general case magnetic reconnection can occur in a magnetic configuration without X-points points as well (e.g. see for a review [28]). More complex view on the flare physics assumes a few stages (at least two) characterized by different peculiarities of magnetic field dynamics and topology.

One of the famous scenario of a 3D flare magnetic reconnection is the tether-cutting magnetic reconnection (TCMR). This model was discussed by [25], where two systems of crossed magnetic field lines (observed as a sigmoid in the soft X-rays) interact in the PIL forming a small-scale sheared arcade below a reconnection site. A large-scale erupting magnetic structure above a reconnection site is also formed. In [21] it was demonstrated the possibility of the TCMR in a solar flare by using multiwavelength observations and nonlinear force-free extrapolation of the magnetic field. Another example is given in [36, 37]. Possibility of a CME triggering by the TCMR process was presented in [3], where a numerical MHD modeling was performed. In this work a two-stage scenario was discussed. A magnetic flux rope firstly is formed due to TCMR, then the torus instability triggers an eruption of the flux rope, and the flare energy release happens behind the erupting flux rope in the frame of 3DSM.

Another two-stage flare model was discussed in [29]. The flare energy release is composed of two main stages. The first one is the so-called 3D “zipper reconnection” spreading along an initially sheared coronal arcade without or with an embedded flux rope above the PIL. The main observational peculiarity is the initial elongation of flare ribbons and parallel motion (“zipping”) of two emission sources (two opposite loop footpoints) along the PIL. In this model the zipping effect results from the 3D magnetic reconnection. The subsequent stage (called as the “main stage”) is the quasi-2D reconnection in the corona due to a flux rope eruption and stretching of overlying magnetic field lines. The second stage results in flare ribbons

that mainly spread away from the PIL. The transition from the quasi-parallel (relative to the PIL) motion of paired hard X-ray (HXR) sources to the quasi-perpendicular motion is indeed observed in a number of solar flares (e.g. [11, 18, 46]). However, we are not aware of observational works that would provide a combined detailed analysis of the two discussed stages of magnetic reconnection, the dynamics of magnetic field and flare emission sources, and compare them with the kinematics of an erupting flux rope.

Despite numerous observational and theoretical studies of solar flares there is a lack of important information about the magnetic field dynamics during the flare impulsive phase due to a low temporal resolution of available vector magnetograms. There is also not enough detailed multiwavelength observational studies clearly showing different regimes of flare energy release during the impulsive phase. Do we really have a transition from one type of magnetic reconnection to another? This question needs in detailed observational studies supported by information about the magnetic field dynamics.

In this work we present a detailed observational case-study of a near-the-limb eruptive solar flare with a pronounced filament (flux rope) eruption and CME. The main physical aim is to investigate the morphology, dynamics and connections between emission sources observed during the flare impulsive phase in the context of magnetic field dynamics connected with the possible regimes of magnetic reconnection. We will focus on a few observational aspects of the flare energy release connected with the magnetic field restructuring. We address three main research tasks:

1. To study magnetic field dynamics around flare emission sources using 45-seconds line-of-sight (LOS) magnetograms of the Helioseismic Magnetic Imager (HMI) [30], onboard the Solar Dynamics Observatory (SDO) [26], to resolve changes of the magnetic field horizontal component on a time scale of the flare impulsive phase ( $\sim 10$  min);
2. Using high-cadence HMI filtergrams with a temporal resolution of 1.8 s to study dynamics of the photospheric flare energy release sites comparing with the temporal and spatial dynamics of X-ray emission sources;
3. To study the overall dynamics of the flare energy release in order to find evidences for the two (or more, if available) stages connected with peculiarities of magnetic reconnection. The most important thing is to connect the observed magnetic field dynamics with these stages.

More comments about the reasons to consider these tasks and data sets are given in the next section.

The paper is organized as follows. Section “Event selection and data” describes a number of criteria used to select a solar flare for our study. In the subsequent section “Overview of the selected flare” we discuss

general observational properties of the selected flare seen in different wavelength ranges. An analysis of 45-seconds HMI LOS magnetograms is described in the section “Investigation of magnetic field dynamics using hmi line-of-sight magnetograms,” and in the next section “Spatial structure of magnetic field disturbances versus morphology of the emission sources” we compare time differences of LOS magnetograms with the Atmospheric Imaging Assembly (AIA) [19] and the Reuven Ramaty High-Energy Solar Spectroscopic Imager (RHESSI) [20] imaging data. In the next section HMI vector magnetograms are analysed. Then, investigation of the photospheric emission source dynamics is presented in the subsequent section. In the last section we summarize and discuss briefly the analysis results obtained.

### EVENT SELECTION AND DATA

In this section we briefly describe some observational data used and the reasons why we selected the particular flare for analysis. One of the key interests in studying solar flares is to investigate spatial structure of the flare energy release developing due to magnetic reconnection. Flare emissions registered in different wavelength ranges are generated by different particular physical processes. In this research we conduct multi-wavelength analysis of the flare energy release during the impulsive phase of an eruptive flare event which is selected according to some reasons.

In order to solve our tasks we have first to find a solar flare which was observed by the certain observatories and which can exhibit physical effects that we want to find and investigate. We are interested in high cadence observations of magnetic field dynamics and changing morphology of flare emission sources as we want to trace peculiarities of magnetic reconnection dynamics. In particular we want to find a transition from one reconnection regime to another in the case of eruptive flares.

We have found a solar flare of GOES X4.9 class occurred on February 25, 2014, with the start at 00:39 UT and peak at 00:49 UT (according to the one-minute GOES data). This time interval is by definition called the flare impulsive phase [4]. This flare was previously investigated by [7] where the authors have shown that the magnetic field topology was in the frame of the TCMR scenario at the initial stage. However, there were no details about subsequent flare energy release and associated dynamics of the magnetic field. Moreover, we found some hints about the two-stage impulsive phase (see below in the next section). Thus, our research tasks are addressed to this particular solar flare revealing initial TCMR topology. Results from the cited paper will be also used for interpretation of our analysis. From our point of view this solar flare is an excellent example to study peculiarities of the energy release during the TCMR process. We consid-

ered the following main reasons to study this solar flare:

1. A solar flare was eruptive with the well-developed CME whose formation and dynamics is clearly seen in the low solar corona by SDO/AIA and the Sun Watcher using Active Pixel System detector and Image Processing (SWAP) onboard the Project for Onboard Autonomy 2 (PROBA2, [12, 33]). We were able to find exact positions of the eruptive structure and flare loops;

2. A solar flare was located close to the solar limb. Firstly, it is important as we are able to trace an eruption with the minimal projection effect. Secondly, in a near-the-limb position, the observed LOS magnetic field predominantly consists of the horizontal (tangential) component, which is of particular interest to us;

3. We need in sufficiently intensive HXR emission fluxes in the energy band of 50–100 keV, which is usually associated with the bremsstrahlung HXR emission of accelerated electrons from the low solar atmosphere. High count rate is necessary to reconstruct HXR images in this energy band with the highest possible temporal resolution. Presence of the HXR emission is an important attribute of the well-developed magnetic reconnection which produces energetic nonthermal electrons;

4. The selected flare was two-ribbon with the photospheric energy release concentrated in the two sources presumably located on opposite sides of the PIL. In this case we ignore complex magnetic field topologies like in the tripple-ribbon, circular-ribbon flares and so on;

5. The flare produced strong photospheric emission sources seen in the HMI filtergrams. We need in this data in order to have high-cadence data of photospheric impacts indicating the strongest flare energy release sites. This will help to find initial photospheric energy release sites and compare them with the regions of magnetic field changes;

6. Location of the two flare ribbons allows to investigate dynamics of the LOS magnetic field in the inter-ribbon space, where the PIL is located and there are no significant disturbances of magnetograms by the flare emission sources. Here we expect the strongest change of the horizontal magnetic field (which is dominant in LOS magnetograms for pre-limb regions);

7. Duration of the flare impulsive phase was large enough. Large flare duration is necessary to use as much as possible 45-seconds HMI LOS magnetograms per flare time to investigate magnetic field dynamics. We think that we need in time period at least 5 min when the HXR emission (50–100 keV) is observed.

In this work we use the following solar space-based instruments providing us with the necessary data:

1. RHESSI allows to reconstruct X-ray images in broad energy ranges above 3 keV. We will perform an analysis of X-ray images with the aim of studying the

dynamics of high temperature ( $T > 10$  MK) plasma and accelerated electrons in the flare region in the energy range of 6–100 keV where count rates are sufficiently strong to achieve good temporal resolution. The nominal temporal resolution of RHESSI is 4 s, which equals to the spacecraft rotation period around its axis. The angular resolution of the finest subcollimator grids is 2.26 arcsec [14, 20]. Additionally, we use temporal profiles (and its time derivative) of solar X-ray emission in the 1–8 and 0.5–4 Å bands detected with the X-Ray Sensor (XRS) onboard the Geostationary Operational Environmental Satellites (GOES) with a 3-second cadence;

2. Extreme ultraviolet (EUV) images in the 94 Å channel (mainly emission of Fe XVIII at  $T \sim 6.3 \times 10^6$  K) from the Atmospheric Imaging Assembly (AIA, [19]) onboard SDO will be used to determine magnetic field geometry and spatial structure of plasma heated in the flare energy release region. The temporal cadence of AIA EUV images in one channel is 12 s and the angular resolution is 1.2 arcsec (0.6 arcsec/pix). We also will use EUV images from the AIA 171 Å channel (mainly emission of Fe IX at  $T \sim 0.6 \times 10^6$  K) to determine and analyze kinematics (temporal profiles of height, velocity, and acceleration) of an eruptive structure associated with the flare. Additionally, for this purpose we will use the EUV images of the PROBA2/SWAP in the 174 Å channel, which has a wider field-of-view (FOV) of  $1.7R_{\odot}$  (compared to  $1.3R_{\odot}$  for AIA) to determine the kinematics of the eruptive structure at higher altitudes (in other words, for a longer time period). The angular pixel size of SWAP is 3.17 arcsec and the cadence for the time interval considered is 110 s;

3. Magnetograms, dopplergrams, and intensity maps from HMI [30] with 45 s cadence do not allow to make a detailed direct comparison with other observational data (for example, 4 s for RHESSI and 12 s for AIA). In this work, we propose to use HMI difference filtergrams (with the temporal resolution of 1.8 s) for identification of the earliest photospheric perturbations in the flare impulsive phase, for the detection of dynamics of the photospheric energy release, and for the accurate comparison of the photospheric emission sources with other observational data obtained in different bands of the electromagnetic spectrum. Filtergram processing methods which we will use in this work are presented in [34, 35] and are based on subtracting the corresponding (certain polarization and wavelength channel) pre-flare filtergrams from the flare one.

## OVERVIEW OF THE SELECTED FLARE

In this section we discuss the main observational peculiarities of this flare before we start a more detailed analysis. The flare site was located in the NOAA active region (AR) 11990, close to the east solar limb, with the approximate heliographic coordinates S12E82

(according to the NOAA GOES XRS reports, <https://www.ngdc.noaa.gov/stp/space-weather/solar-data/solar-features/solar-flares/x-rays/goes/xrs/>) and the helioprojective coordinates ( $-929''$ ,  $-211''$ ) (according to the RHESSI quick-look image catalog [http://hessi.ssl.berkeley.edu/hessidata/metadata/qlook\\\_image\\\_plot/2014/02/25/](http://hessi.ssl.berkeley.edu/hessidata/metadata/qlook\_image\_plot/2014/02/25/)).

The flare X-ray temporal profiles obtained from the RHESSI data are presented in Fig. 1a. The highest available energy band is 800–7000 keV, but in our study we will use only the energy bands in the range of 6–100 keV covering both thermal and nonthermal emissions. Moreover, this energy range is selected as it has sufficient count statistics to reconstruct qualitative images with high temporal resolution of 12 s, which is comparable with the AIA cadence. From the count rates one can see that the HXR (above 50 keV) temporal profiles consist of several peaks with the most intense one occurred around 00:45 UT.

By comparing images from different instruments in Fig. 1b, we show the basic morphological peculiarities of the flare energy release spatial structure seen during the impulsive phase. A background is the EUV AIA 94 Å image selected to show an appearance of the flare loop(s) with the bright footpoints and formation of the eruptive structure developed into the CME. The X-ray images were reconstructed using the EM algorithm [14]. By the contours of different colors we present 6–12 keV SXR images for the two time points: one around 00:41~UT (approximate eruption onset) and another one around 00:45 UT (the HXR peak). One can see that the SXR loop(s) experienced an apparent displacement corresponding to displacement of the photospheric emission sources (from HMI filtergrams) shown by grey color for the time range of 00:43–00:46 UT. This motion, approximately from the north to south, called “zipping” is shown in panels c and e1 in more details. Fig. 1c presents dynamics of the HXR and SXR sources revealing the “zipping” motion and the rising expanding SXR source.

In Figs. 1d1–1d6 we present comparison of the photospheric emission sources from the HMI filtergrams with the RHESSI 6–12 and 50–100 keV contour maps. The photospheric emission sources were obtained by subtracting corresponding pre-flare HMI filtergrams from the flare ones. One can see that the centroids of the HXR sources (up to three centroids) was near the positions of the photospheric disturbances developing from initial compact emission kernels to flare ribbons. However, there is no absolute correspondence between emission sources of these two types. Not exact coincidence can be easily explained by different dynamic ranges, expositions, spatial resolutions of the HXR and Optical telescopes. However, approximate spatial correspondence should be considered as important observation confirming possible common origin of these emissions connected with nonthermal electrons injecting into lower solar

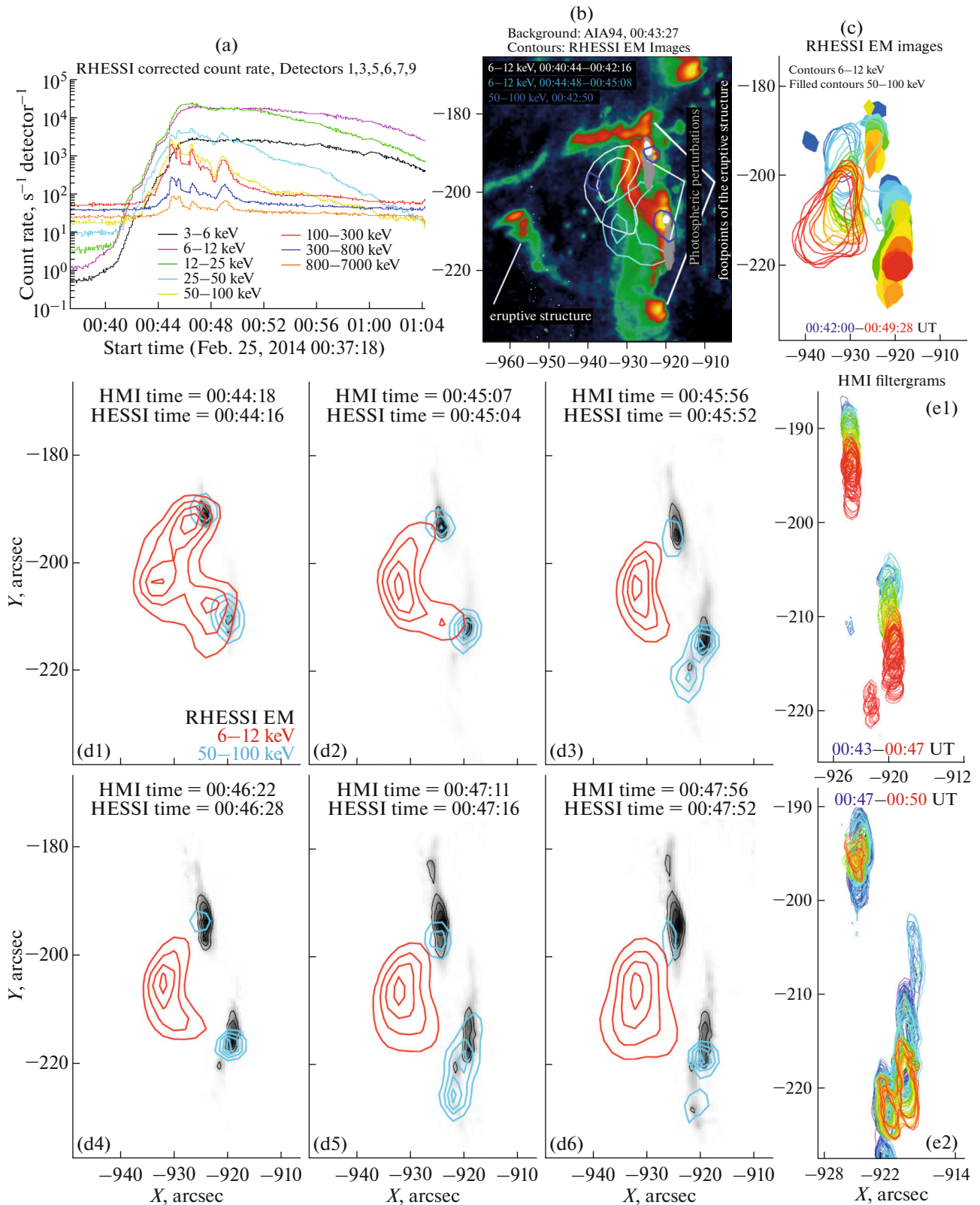


**Fig. 1.** General overview of the X4.9 flare on February 25, 2014: (a) temporal profiles of X-ray emission detected by RHESSI; (b) AIA 94 Å image comparing with the RHESSI X-ray contour images and HMI photospheric emission sources at 00:43–00:45 UT; (c) temporal dynamics of the RHESSI X-ray sources in 6–12 and 50–100 keV; (d1–d6) comparison of the X-ray sources with the HMI photospheric emission sources; (e1–e2) temporal dynamics of the HMI photospheric emission sources.

atmosphere. In this case photospheric disturbances can be considered as a proxy of the precipitating non-thermal electrons.

The “zipping” motion of the photospheric sources is clearly seen in Fig. 1e1, where the contours mark different time intervals (shown by different colors) within the time interval of 00:43–00:47 UT. Panel e2 presents dynamics of the photospheric perturbations for the time interval of 00:47–00:50 UT. One can note that the source sizes are larger comparing with the e1 and there was no clear “zipping” in this time interval. Detailed analysis of the photospheric emission sources parameters will be presented below in the paper.

The initial photospheric impacts (marked by white color in Fig. 1b) were detected around the EUV loop footpoints, where the first HXR 50–100 keV sources were also located. It is also important to notice that all high energy processes were developed under the erupting magnetic structure.

To sum up these brief data, we can say that the found solar flare presents hints on two-stage energy release: the “zipping” stage and a subsequent stage of the expanding coronal SXR emission source. In the following sections there will be more confirmations of the two-stage flare impulsive phase.

#### INVESTIGATION OF MAGNETIC FIELD DYNAMICS USING HMI LINE-OF-SIGHT MAGNETOGRAMS

HMI makes spatially resolved measurements of the line-of-sight magnetic field, the full vector of magnetic field, the intensity and Doppler velocities of the plasma in the solar photosphere. The principle of magnetic field measurement is based on the Zeeman effect of magnetically sensitive line Fe I (6173 Å) for different polarizations in six wavelength channels. Images are recorded by two separate cameras, producing a sequence of filtergrams (level-1 data) at different wavelengths and different polarizations with a cadence of about 3.6 s for individual cameras (or 1.8 s for both cameras). Then all standard HMI observables are reconstructed from these filtergrams based on the HMI pipeline [6].

The total time resolution of the standard vector magnetograms is 720 s and it is not enough to catch sharp changes of magnetic field during the flare impulsive phase. There are also a bit noisy 135-seconds vector magnetograms (e.g. [36, 40]) allowing to plot a few magnetograms per impulsive phase with the duration of 5–10 min. Such data is also not enough for our tasks. With the better time resolution of 45 s, it will be possible to trace changes of the line-of-sight component of magnetic field (in HMI LOS magnetograms) and compare the locations of the strongest jumps of the magnetic field with the radiation sources in various bands of the spectrum. However, to interpret the obtained information correctly one needs to

understand which component (vertical or horizontal) is dominant in LOS component. From this point of view, a near-the-limb position of the solar flare is preferable as the horizontal magnetic field gives the main contribution to the LOS magnetic field. It is known that this component subjects to the greatest and fastest changes around the PIL (e.g. [1, 27, 36, 40, 41]), while the vertical (radial) component is less affected by magnetic restructuring. Thus, we expect that 45-seconds HMI LOS magnetograms will allow to study magnetic field restructuring. Then by analyzing the standard 720-seconds magnetograms we will be able to discuss changes of the total magnetic field vector taking into account real temporal dynamics of the magnetic field deduced from 45-seconds data.

In Figs. 2a–2f we show the running time differences of the HMI LOS magnetograms. Saturated regions of red color with the sharp edges (visually corresponding to strong color gradient regions) correspond to the photospheric emission sources seen in the HMI filtergrams (Figs. 1d–1e) co-spatial with the ribbons. Magnetic field values in these regions was not measured properly due to Fe I line distortions connected with the flare energy release seen as emission enhancement in the different polarization modes and wavelengths (around Fe I line).

In the interribbon space one can see (Fig. 2a) an appearance of weaker perturbations of the LOS magnetic field. Here we assume real measurements of the magnetic field values. The amplitude of this perturbation was maximal around the HXR peak time (Fig. 2c). There are a few reasons to consider this perturbations as reasonable data. First of all, we analyzed temporal dynamics of the Fe I RCP and LCP line profiles in the different groups of points located in the different regions (flare ribbons and ROI1 and 2). It was found that distortions of the Gaussian-like profiles was sufficiently small in the selected ROIs during the time moment when we observed maximum of the photospheric emission. In other words we have gaussian lines with different depths and widths and hmi pipeline works well in the case of determination of the LOS component.

We mark the place of the strongest perturbations as the region-of-interest 1 (ROI 1). The ROI 2 corresponds to the place of magnetic field change occurred after the HXR peak. This perturbation is more diffusive (best seen in e and f) comparing with the localized one in the ROI 1.

The total change of the LOS magnetic field is shown by the difference map (Fig. 2g), where the pre-flare magnetogram was subtracted from the post-flare one. The region of the magnetic field change was mostly in the compact interribbon space. However, there were diffusive regions of the weaker LOS magnetic field change, with some of them to be distant and associated with the flare loop footpoints. The described difference map confirms the fact that these



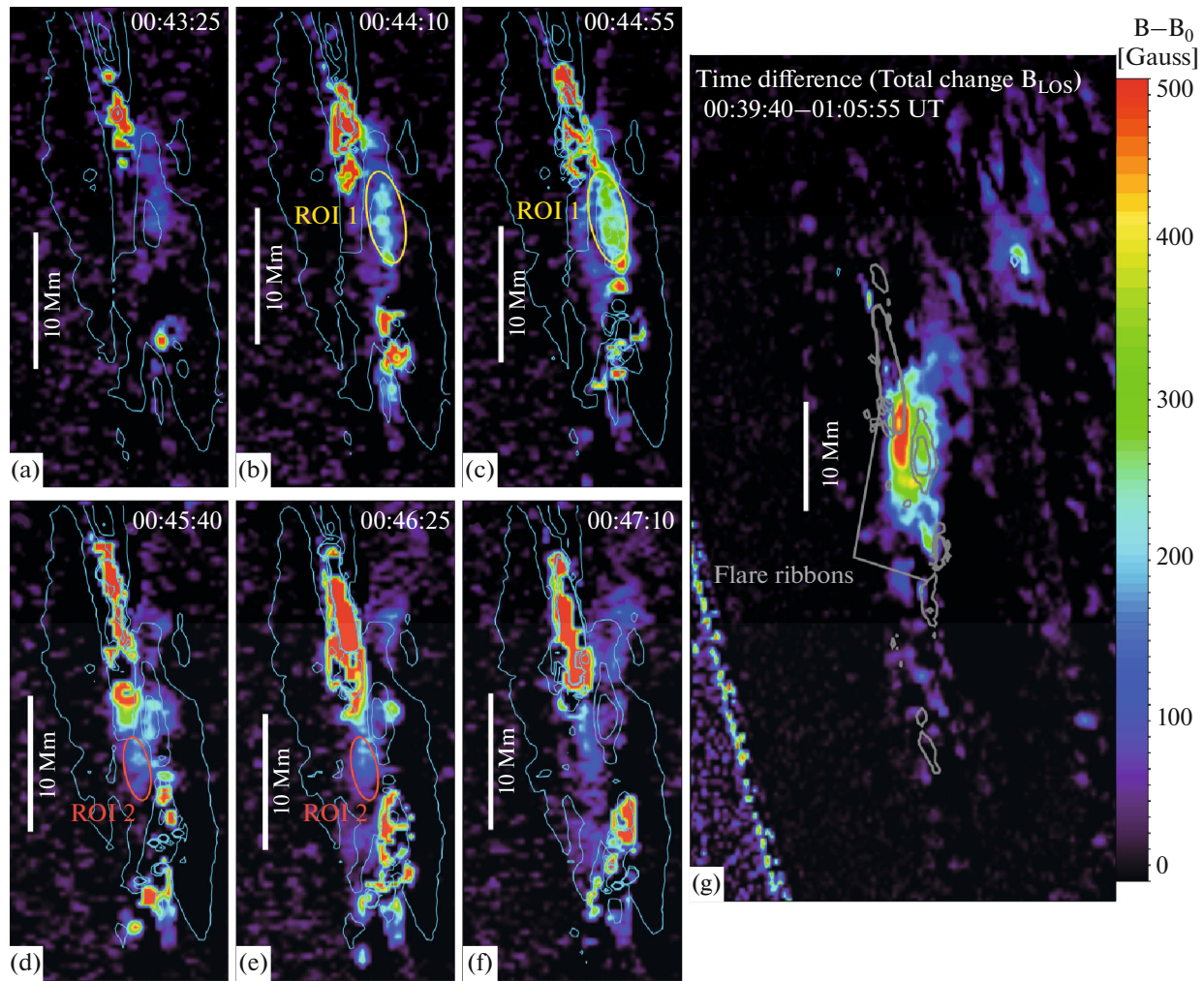


**Fig. 2.** Sequence of the running time differences of the HMI LOS magnetograms (a–d) and the total change of the LOS magnetic field (g). Two ellipses mark regions of the enhanced LOS magnetic field in the interribbon space (where the PIL is possibly located). Cyan contours in (a–) correspond to the levels of 400, 800, and 1000 Gauss of the LOS magnetic field. Gray contours in (g) correspond to the levels of 800 and 1000 G of the LOS magnetic field. Some of these gray contours mark (by gray lines) positions of the flare ribbons impacts due to incorrect determination of the LOS field. Horizontal dashed lines in (a–f) show the observational slit used to reconstruct the time–distance diagram (shown in Fig. 3a) of the LOS magnetic field dynamics in the interribbon space.

interribbon perturbations of the LOS magnetic field are not artifacts as the spatial distribution of magnetic field was stabilized after the flare contrary to the flare induced perturbations having a transient impulsive nature.

Temporal dynamics of the changing LOS magnetic field is presented in Fig. 3a. Panel a is the time–distance diagram for the observational slit crossing the interribbon space (the horizontal dashed line in Figs. 2a–2f) where the maximal jump of the magnetic field was detected. Fast change of the magnetic field is evident from this plot. For the line  $Y = 14$  Mm (crossing the region of the strongest LOS magnetic field change) one can see a jump approximately from 800 to 1300 G, whereas for the line  $Y = 10$  Mm (crossing the southern interribbon region of the weaker changes) we

found a sharp jump approximately from 300 to 700 G. This is in favor of the initial flare energy release and corresponding magnetic field change started around the place with strong horizontal magnetic field. Then we observe that the magnetic restructuring affects on the other regions with weaker magnetic field.

An important thing is a transition from one stable pre-flare distribution of the magnetic field along the artificial slit to another post-flare distribution resulted from the flare magnetic restructuring. We do not see strong transient distortions of the LOS magnetograms for this slit position. It could be interpreted as there were no observable artifacts due to flare impacts.

Another interesting thing is the inclined contour in the time–distance (TD) plot (Fig. 3a) during the flare impulsive phase toward the limb direction and roughly

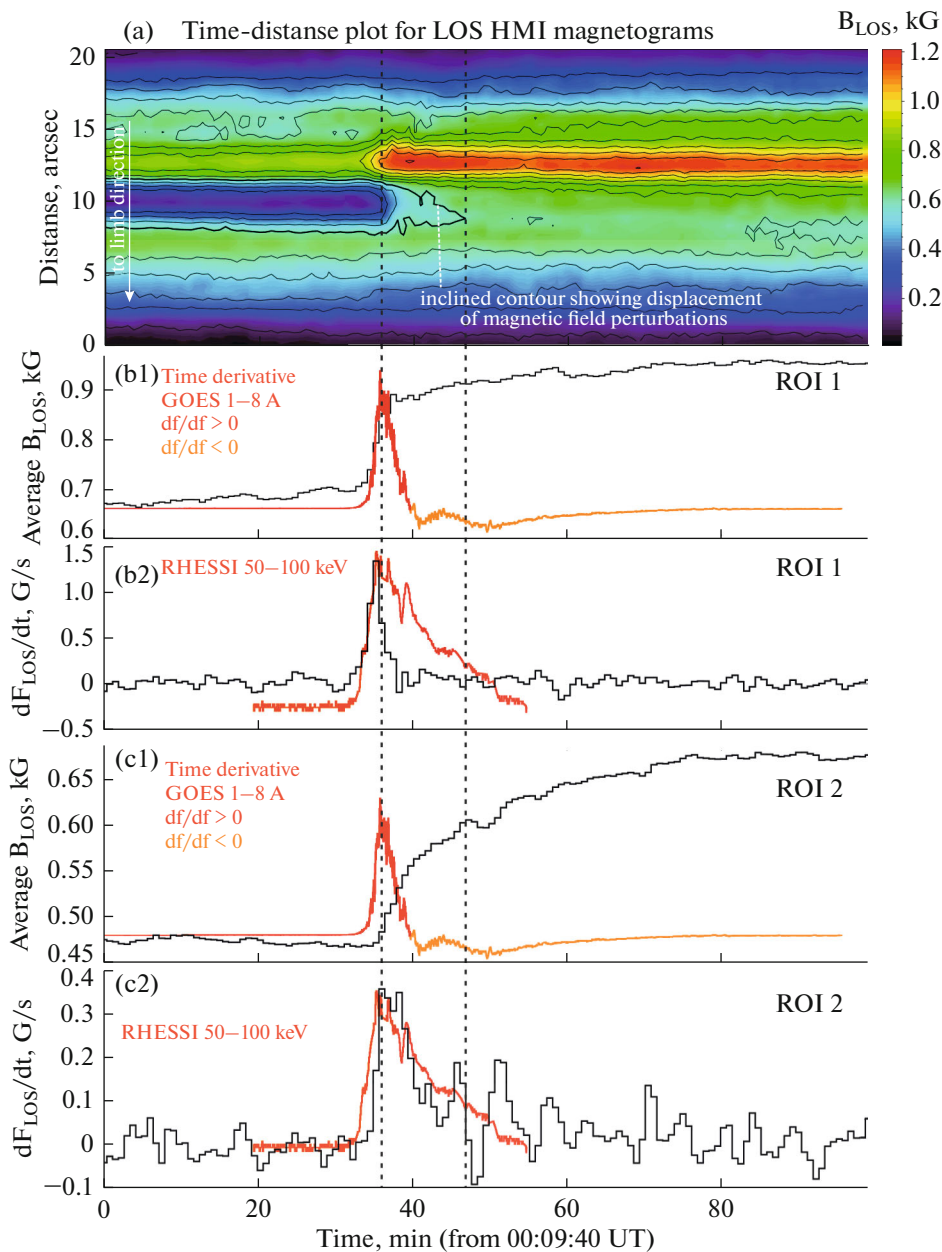


**Fig. 3.** Temporal dynamics of the magnetic field derived from the HMI LOS magnetograms. Panel (a) shows a time-distance diagram obtained from the observational slit (shown by the horizontal line in Fig. 2) applied to the HMI LOS magnetograms. Here we mark a special contour showing an expanding interribbon perturbation of the magnetic field between two points in time (indicated by the vertical lines). The LOS magnetic flux for two ROIs (ellipses in Fig. 2) are in panels (b1) and (c1). The corresponding time derivatives of these fluxes are in panels (b2) and (c2), respectively. The temporal profiles are compared with the time derivative of the GOES 1–8 Å flux (b1 and c1) and 50–100 keV RHESSI count rate (b2 and c2).

corresponding to the direction along the ribbons. We interpret this peculiarity as an apparently moving magnetic field perturbation along the PIL possibly corresponding to the “zipping” motion. The estimated velocity along the observational slit is about 5 km/s. However if we assume that this velocity is the X projection of the main velocity vector along the PIL, then we can obtain more real value of 20–40 km/s for the angle value about 80 degrees (which is the helio-

graphic longitude of the flare location). It is close to the “zipping” velocity values (approximately 30 km/s, see Figs. 6c1–6c2) for the emission sources in the low solar atmosphere. Thus, we state that using even 45-seconds HMI magnetograms we are able to catch magnetic field dynamics during the flare impulsive phase. However this observation is quite discussible. For example, this zipping motion can be a kind of expansion.



In other panels (Figs. 3b, 3c) we show the averaged LOS magnetic field values and their time derivatives obtained for the ROI 1 and ROI 2. For the case of the strongest magnetic field perturbation one observes a jump of the averaged LOS magnetic field approximately from 700 Gauss to 900 Gauss (b1), whereas for the ROI 2 there was a change from 460 to 600 Gauss (c1). The difference between the magnetic field dynamics is more clear when considering the time derivatives of the averaged LOS magnetic field in b2 and c2. The maximal value for the ROI 1 was about 1.5 Gauss/s that is 5 times larger than for the ROI 2 (about 0.3 Gauss/s). One can also see that the magnetic field disturbance was more impulsive (about 5 min) in the ROI 1, whereas in the ROI 2 the more gradual (about 10 min) disturbance developed in the time period (between two vertical dashed lines) when there was a displacement of the LOS magnetic field perturbation along the flare ribbons (see the inclined contour in panel a).

The temporal profiles showing dynamics of the averaged LOS magnetic field in two ROIs are also compared with the temporal profiles of the RHESSI 50–100 keV count rate and GOES/XRS 1–8 Å SXR flux. The maximal value of the ROI 1 magnetic field time derivative was around the main HXR peak. Then the subsequent HXR peaks were associated with the changing magnetic field in the ROI 2 (c2).

Let's sum up the results of the HMI LOS magnetogram analysis. The near-the-limb position of the selected flare gives us an opportunity to discuss the horizontal magnetic field dynamics, and we were able to resolve some peculiarities of this dynamics during the flare impulsive phase. There was a sharp irreversible enhancement of the magnetic field value in the interribbon space and we found the expanding magnetic field perturbation along the flare ribbons, possibly connected with the “zipping” effect. The strongest magnetic field perturbation was associated with the most intensive HXR peak and the flare onset was associated with the strongest magnetic field. Possibly we observe two magnetic field change regimes associated with the two stages of the flare energy release: the first short duration (~5 min) initial zipping-like magnetic reconnection stage and the subsequent more prolonged (>10 min) eruptive stage.

#### SPATIAL STRUCTURE OF MAGNETIC FIELD DISTURBANCES VERSUS MORPHOLOGY OF THE EMISSION SOURCES

In this short section we discuss spatial structure of the flare energy release sites seen by different instruments taking into account information about the LOS magnetic field dynamics found in the previous Section. Comparison of the different emission maps with the regions of the magnetic field change is shown in Fig. 4.

Black thin isocontours in Figs. 4a–4c show the regions with magnetic field change rates of 0.4 and 2 Gauss/s. In the panel d we show contours (thin black) of the total LOS magnetic field change (as in Fig. 2) calculated as a difference between post-flare and pre-flare LOS magnetograms. All emission sources and magnetic field data in Figs. 4a–4c are plotted for the time intervals closest to the time point of the background AIA 94 Å image. The coronal SXR emission sources associated with the hot thermal plasma were located slightly (a few arcseconds) above the EUV loop(s) and well below (tens of arcseconds) the eruptive structure. It is logical from the point of view of the TCMR scenario. Indeed, the TCMR geometry assumes the eruptive structure to be formed above an initial reconnection site. The lower compact magnetic loops are also resulted from the TCMR reconnection [21].

The LOS magnetic field perturbation started to grow and develop (Figs. 4a–4c) in the region between the emission (HXR, photospheric and EUV) sources located in the footpoints of the flare loop(s) seen in the 6–25 keV SXR and AIA 94 Å channel. The largest amplitude of the total magnetic field change seen in the panel d is also concentrated in the place between footpoints of the flare loop(s).

#### INVESTIGATION OF MAGNETIC FIELD DYNAMICS USING HMI 720-SECOND VECTOR MAGNETOGRAMS

The LOS magnetograms in application to the near-the-limb solar flare allows us to discuss only dynamics of the LOS component of the horizontal photospheric magnetic field. In this section we will analyze the standard HMI vector magnetograms. Their temporal resolution of 720 s is not enough to resolve dynamics during the flare impulsive phase. However, taking into account our knowledge about the magnetic field obtained from the 45-seconds LOS magnetograms, one can discuss changes of the magnetic field vector on this time scale.

Another important problem is impossibility to resolve the  $\pi$ -disambiguity for the photospheric magnetic field measured near the solar limb. Thus, to investigate magnetic field spatial distribution we will use only original data without projection onto the heliographic grid with determining magnetic field components in the spherical coordinates.

Time-distance plots made for vector magnetograms are shown in Figs. 5a–5d and the observational slice (artificial slit) intersecting the interribbon space is shown in Figs. 5A–5B. Changes in the flare region were the most significant for the LOS component (red contours in A and B) and magnetic field azimuth (white-black background in A and B). Because of the absence of the  $\pi$ -disambiguity correction we used special visualization to identify magnetic structure of our

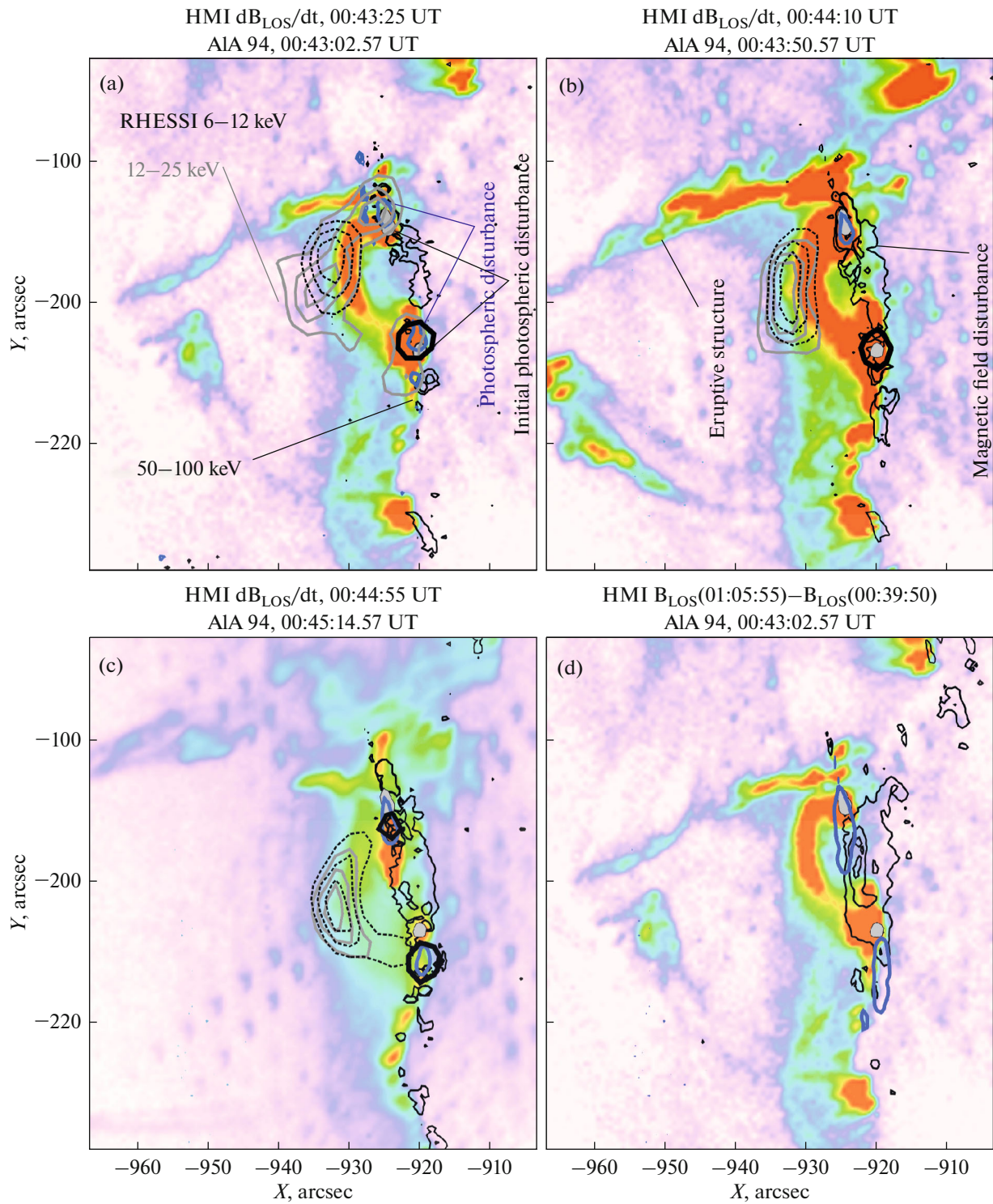


**Fig. 4.** The background images show the AIA 94 Å images. The thin black contours in (a–c) correspond to  $dB_{\text{LOS}}/dt$  levels of 0.4 and  $2 \text{ G s}^{-1}$  ((a–f) in Fig. 2). The thin black contours in (d) show regions of the LOS magnetic field total change with the levels of 100, 300, and 500 G (Fig. 2g). The dotted and gray contours (40, 60, and 80%) show the RHESSI X-ray sources in the energy bands of 6–12 and 12–25 keV. The thick black contour marks the 50–100 keV X-ray source at the level of 50% from its maximal brightness. The photospheric emission sources derived from the HMI filtergrams are shown by the blue contours for times closest to the selected AIA images. The gray filled contours define the initial photospheric emission sources.

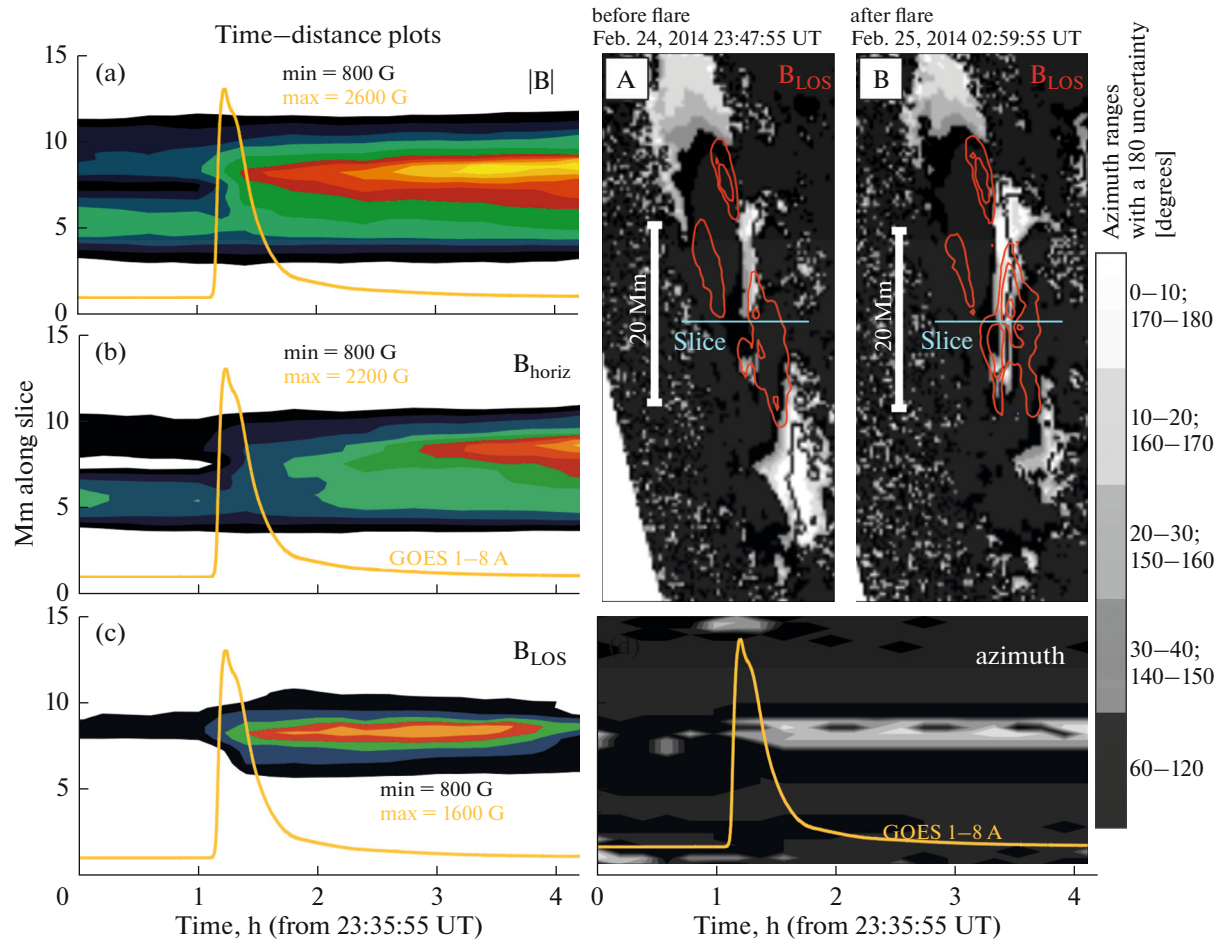


**Fig. 5.** Representation of the analysis of the HMI vector magnetograms. Panels (a–d) show time-distance (TD) plots for three different components (a–c) of the magnetic field and azimuth (d) with  $\pi$ -disambiguation. These TD-plots are made for the observational slit plotted in (A) and (B), where the azimuth (background) map with contours of LOS magnetic field is shown. These two panels correspond to the pre-flare and post-flare times.

interest. We know that the flare ribbons are oriented approximately in the north-south direction, then we could assume that magnetic field azimuth in the vicinity of the flare ribbons should be around two values 0 and 180 degrees due to unresolved  $\pi$ -disambiguation. This expectation is connected with the fact that we assume strong magnetic shear in the PIL region (the usual situation for the powerful solar flares). To visualize the sheared magnetic structure we decided to mark by white and gray colors pixels with values lying in the certain azimuth ranges (see the white-black bar on the right in Fig. 5), where each color corresponds to two ranges with difference of 180 degrees. From these two maps we see that there was elongated sheared structure which became larger after the flare. The important thing is the appearance of the strong shear around the region where enhancement of the LOS component was detected. A time scale of the azimuth jump at the PIL in the interribbon space (Fig. 5d) is of the same order as for the LOS magnetic field component.

The TD-plot in Fig. 5a is shown for the magnetic field absolute value. We observe a sharp change of the

magnetic field structure around the flare impulsive phase and a subsequent gradual variation after the flare. These fast and slow components are likely connected with the following processes. Initially there was a fast change of the horizontal magnetic component perpendicular to the PIL (which is observed as the LOS component in the panel c). One observes the double growth of the LOS component. The magnetic field component in the sky projection plane (marked as  $B_{\text{horiz}}$  in Fig. 5b) experienced slow dynamics with its peak when there is already a decay of the LOS component. We suggest that such dynamics is due to relaxation of the postflare arcade formed due to eruption. In this case the shear angle started to decrease.

The HMI 720-seconds vector magnetograms confirm fast variations around the flare onset found in 45-seconds LOS magnetograms. Moreover, the magnetic field variations and the flare onset emission sources were associated with the sheared magnetic structure. The fast initial magnetic field variations were likely associated with the initial magnetic reconnection of the sheared loops, whereas the gradual long dura-

tional magnetic field changes were due to formation of the less-sheared “post-eruptive” arcade. More details about the two-stage flare energy release will be given by analysis of the photospheric emission sources dynamics.

### INVESTIGATION OF THE ENERGY RELEASE DYNAMICS ON THE PHOTOSPHERE USING HMI FILTERGRAMS AND COMPARISON WITH KINEMATICS OF THE ERUPTION

In this section we discuss analysis of the energy release dynamics observed on the photosphere using HMI filtergrams. Brief discussion of the photospheric emission sources was in the section devoted to the flare overview, where the HXR 50–100 keV emission sources were compared with positions of the photospheric impacts (Figs. 1d1–1d6). We found the double footpoint-like photospheric perturbations associated with the places where electrons precipitated from the coronal sources into the low solar atmosphere. These double sources experienced the “zipping” motion and their area was also variable. In this section we present estimations of different parameters of the photospheric emission sources dynamics. We also compare the found parameters with the dynamics of the magnetic field and different emissions.

In Fig. 6a the temporal profiles of the total intensity in the south (a1) and north (a2) photospheric emission sources are shown. The intensities were calculated for the areas limited by contours plotted for the 50% level relative to the intensity maximum. Data for the cameras 1 and 2 are plotted by black and red colors, respectively. The cyan lines in Fig. 6 correspond to the RHESSI HXR 50–100 keV count rate and the gray histogram is the time derivative of the LOS magnetic flux calculated for the ROI 1 (Figs. 2 and 3). Data in panels a show clear photospheric flare emission enhancement during the first 4 min. A good peak-to-peak coincidence between the photospheric intensity and the HXR count rate was up to the HXR maximum, then we do not see such a good correlation. The thing is that the instrumental oscillations connected with the scanning of the Fe I line were significant and distorted the flare emission temporal profile.

In panels b we present the temporal profiles of the nominal photospheric optical emission flux density from the observed sources. These temporal profiles are ratios of the total emission intensity to the source area (panels d) measured in HMI pixels. One can see that such temporal profiles have better correspondence with the HXR temporal profile. To sum up analysis of the panels a and b we can state that the energy release connected with the HXR and photospheric emissions was co-spatial and co-temporal. The maximum of the photospheric and the HXR emissions was at the same time when we registered the peak of the magnetic field change rate in the ROI 1 (Fig. 2). The magnetic field change in the ROI 2 was

maximal during the decay of the HXR and photospheric emissions (b1).

Characteristics of the photospheric emission sources motions are shown in Figs. 6c1–6c3. We consider only displacement along the  $Y$ -axis (of the helioprojective coordinates) as motion along the  $X$ -axis was negligible due to the north-south orientation of the flare ribbons. Panels c1–c2 show  $Y$  coordinates of the center-of-masses of the north and south emission sources, respectively. Vertical error bars correspond to the  $Y$  sigmas characterizing the size of the photospheric emission sources. Looking at these temporal profiles one can notice that there was the “zipping” motion with the approximate velocity of 25 km/s during the first 3–4 min (approximately from 00:43 UT to 00:47 UT). This time period was associated with the most intensive HXR emission and the significant magnetic field changes around the ROI  $\sim 1$ . Then positions of the photospheric emission sources were stabilized and the magnetic field change rate was less and associated with the ROI 2. The difference between the  $Y$  coordinates of the north and south sources is presented in the panel c3, where the gradual separation between the two flare sources (ribbons) (approximately after 00:46–00:47 UT) is seen. This separation was accompanied by the growth of the SXR 6–12 keV source area (the blue line in c3), calculated as FWHM area in the 50% contour. Such observations show a typical growth of the flare arcade during the eruption when magnetic reconnection develops in the quasi-vertical current sheet behind the erupting structure.

Dynamics of the emission source area (Figs. 6d1, 6d2) shows the following peculiarities. For the “zipping” stage, during the first 3 minutes, the sources were the most compact with their area as small as  $(1-3) \times 10^{16}$  cm<sup>2</sup> for both north and south ones. Then we observe expansion of the photospheric ribbons when there were no significant motions of their center-of-masses. This stage is associated with the growth of the flare arcade.

It also important to compare the dynamics of the photospheric sources with the kinematics of the eruptive structure (which can be seen in Fig. 4 and discussed in [7]). To do this, using jointly the data of SDO/AIA in the 171 Å and PROBA2/SWAP in the 174 Å channels, we first found the temporal profile of the approximate height of the eruptive structure’s leading edge along the cut (artificial slit) with the helioprojective coordinates of the end points (–925”, –199”) and (–1197”, –237”) corresponding to the main direction of the eruptive structure propagation. Error estimates are also obtained, as a standard deviation from the mean with weights in the form of brightness values in the considered local regions along the cut for each image. The regularization method (see e.g. [17, 42, 43]) is used to obtain velocity and acceleration profiles versus time. The SWAP data made it possible to expand the surveyed area (due to the larger FOV) and better track



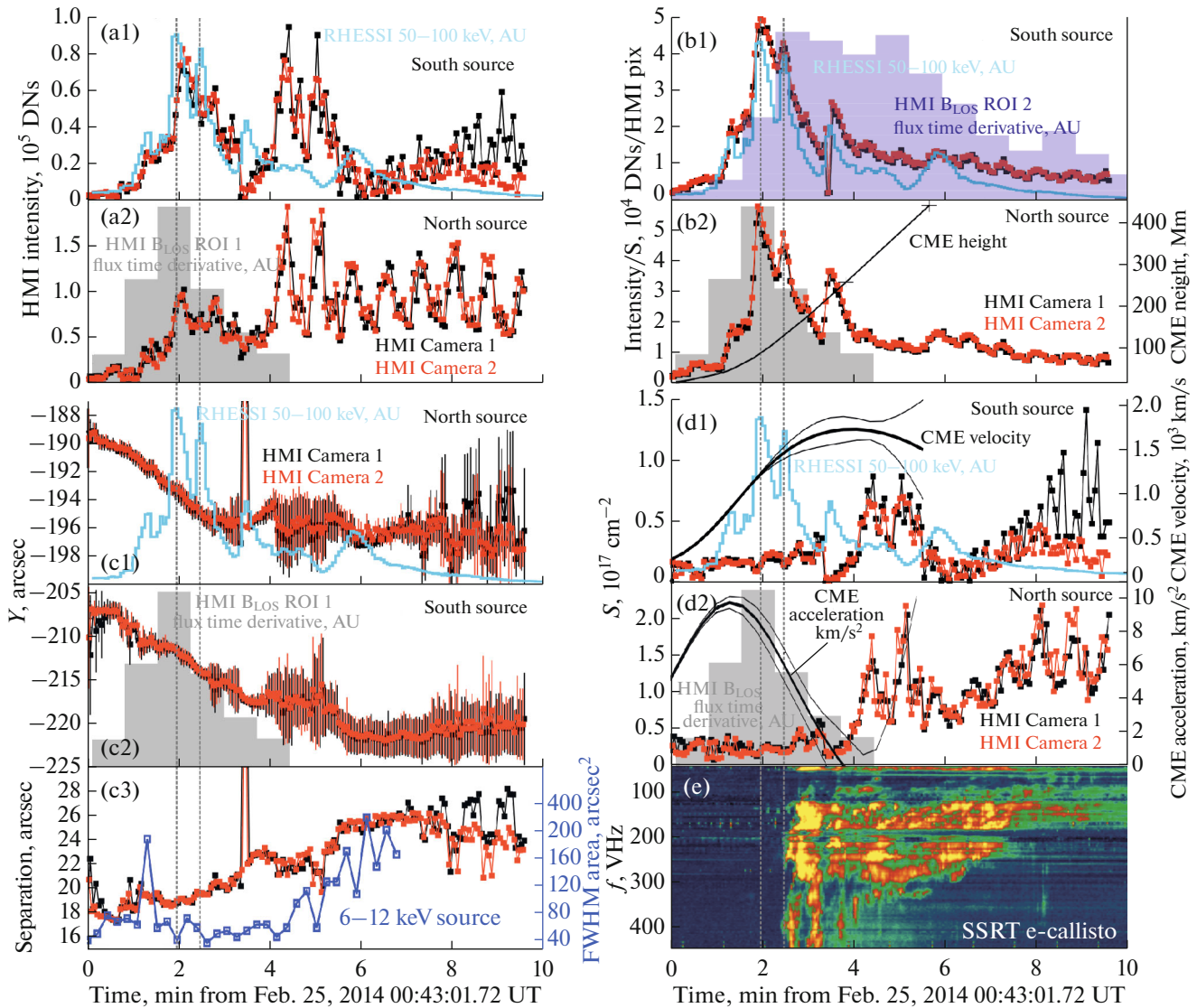


**Fig. 6.** Temporal dynamics of the photospheric emission sources' properties defined from the HMI filtergrams. Panels numbered as 1 and 2 correspond to two characteristics of the south and north photospheric sources, respectively. Data from the cameras 1 and 2 are marked by the black and red colors, respectively. Panel (a) shows the total intensity of the photospheric emission, while (b) presents the specific intensity in DN<sub>s</sub>/HMI pixel (intensity divided by the source area). Dynamics of the emission sources is shown in (c), where (c1–c2) display displacement in the  $Y$ -direction and (c3) shows the distance between the north and south sources. Area of the photospheric sources is shown in panel (d). The last panel (e) presents the metric radio dynamic spectrogram from the SSRT e-Callisto radio spectrometer. Cyan temporal profiles show the RHESSI count rate in the 50–100 keV range. Gray and blue histograms are the time derivatives of the LOS magnetic field fluxes in the ROI 1 and 2, respectively (Fig. 2). Dynamics of the 6–12 keV SXR source area is shown by the blue temporal profile in (c3). The temporal profiles of the eruptive structure height above the photosphere, velocity, and acceleration are shown by the thick black curves in (b2), (d1), and (d2), respectively. The two thin black curves around them indicate the range of estimated errors of these physical parameters.

the peak of the eruption acceleration. The errors of the obtained profiles were calculated by the Monte Carlo method based on the obtained height errors. By numerical integration, inverse height profiles were obtained from the reconstructed velocities and accelerations. The obtained profiles are within the limits of data errors, which confirms the correctness of the obtained kinematic curves (a more detailed description of the developed methodology for determining the kinematics of eruptions will be presented in a separate work).

The temporal profiles of the height, velocity, and acceleration of the eruptive structure's leading edge are shown by the thick solid black curves in Fig. 6b2, 6d1, 6d2, respectively. The error ranges are indicated by two thin solid black curves above and below the thick curves. It can be seen that the accelerated rise of the eruptive structure began before the start of the HXR bursts in the first “zipping” stage of the photospheric sources motions, and the acceleration peak ( $10 \text{ km s}^{-2}$ ) was reached approximately 1.5 min before the main



HXR peak (approximately at 00:44:30 UT) and the main horizontal magnetic field growth rate. This is in good agreement with what was found in the statistical study by [5]. The eruption speed continued to increase after that for about another 2.5 min and reached a peak ( $1700 \text{ km s}^{-1}$ ) approximately at 00:47 UT, after the main HXR peak, approximately at the time when the growth of the flare loop arcade and the second stage of the movement of photospheric (and HXR) sources began. We also note that the approximate transition between the two stages around the 3rd minute was detected when the eruptive structure was as high as 180 Mm above the photosphere that exceeds the size of the entire active region.

To sum up, the obtained results evidence in favor of the presence of two stages of the energy release during the flare impulsive phase (00:39–00:49 UT). The first stage is characterized by the “zipping” motion of compact footpoint-like emission sources in the low solar atmosphere. The most dramatic magnetic field change was also during the first stage. Expansion of the flare ribbons and less pronounced magnetic variations was during the second stage.

In Fig. 6e we show the e-Callisto Siberian Solar Radio Telescope (SSRT) radio dynamic spectrum in the range of 45–440 MHz. The onset of the type III radio bursts (and the subsequent type II radio burst) was around 00:45:30 UT. This time corresponds to the end of the first (“zipping”) stage and beginning of the second stage. An appearance of the type III radio bursts can be interpreted as an indirect marker of the efficient magnetic reconnection in the current sheet below the eruptive structure (as in the SM scenario) and access of nonthermal electrons to the large “open” magnetic structures. Before this, during the “zipping” stage, populations of nonthermal electrons (associated with the strongest HXR bursts) were locked in the relatively low closed magnetic loops.

Finally, Fig. 7 presents dynamics of the X-ray emission sources relative to the photospheric disturbances. The first frame a shows only the SXR loop(s) and HXR footpoints. Then we observe an appearance of the coronal HXR (25–50 keV) emission source (b–c) co-spatial with the SXR loop(s). In the frame d the coronal HXR emission source has the similar intensity comparing with the footpoint sources. At this time we also register an appearance of the type III radio bursts (see Fig. 6e). The maximal integrated HXR flux is observed during the time intervals shown in e–g frames. One can interpret this fact in the following way. The enhanced coronal 25–50 keV emission was connected with the appearance of the quasi-vertical current sheet formed below the eruptive magnetic flux rope (as in SM). Possibly, the large coronal HXR source is connected with the trapped nonthermal electrons in the magnetic loops of the growing flare arcade leading to in-situ plasma heating. Generally, the HXR footpoint emission sources have very good spatial

coincidence with the photospheric impacts. Note also that the coronal HXR emission sources have similar height dynamics comparing with the SXR sources.

## SUMMARY AND DISCUSSION

In this section we present a summary of the observational results, discuss methodological aspects and physics of the flare energy release studied. It is worth reminding that the specific flare was chosen for our analysis to trace magnetic field dynamics with high temporal and spatial resolution and investigate regimes of the flare energy release. Using the favorable location (on the solar disk and close to the limb) of the selected eruptive flare (X4.9 February 25, 2014) and data with high temporal and spatial resolution (HMI LOS magnetograms and HMI filtergrams), it was possible to distinguish two stages of the development of energy release in the flare impulsive phase (before the maximum of SXR emission). Firstly, let’s list the observational results and then at the end of this section we shortly discuss the two founded stages of the flare energy release and possible underlying physical processes.

The main methodological peculiarity of this work is simultaneous usage of the high-cadence 45-second LOS HMI magnetograms and 720-second HMI vector magnetogram to understand magnetic field dynamics on the time-scale of the impulsive phase. The 720-second data and even 135-second vector magnetograms are not suitable for investigation of the magnetic field dynamics during the short impulsive phase. Additional information from the 45-second magnetograms gives around ten data points per the impulsive phase that is enough to catch the main peculiarities of the magnetic field dynamics connected with the flare associated magnetic field restructuring. Applying this methodology to the selected flare we found the following phenomena:

1. The flare onset and the corresponding start of the first stage of the impulsive phase was initiated in the region of the strong sheared magnetic field comparing with the subsequent time intervals. The subsequent flare energy release involves regions with the weaker magnetic field;
2. We found that the strongest magnetic field jump of  $1\text{--}2 \text{ G s}^{-1}$  at the PIL associated with the HXR peak had an approximate duration of 2 min. Due to specific near-the-limb location of the flare site we concluded that the magnetic field horizontal component experienced this jump at the localized region between the flare ribbons with the approximate size of 8 Mm;
3. After the main HXR peak there was a magnetic field restructuring in a larger region with a few times less amplitude comparing with the initial magnetic field jump. This behaviour of the photospheric magnetic field highlights the presence of the two stages of the magnetic reconnection;

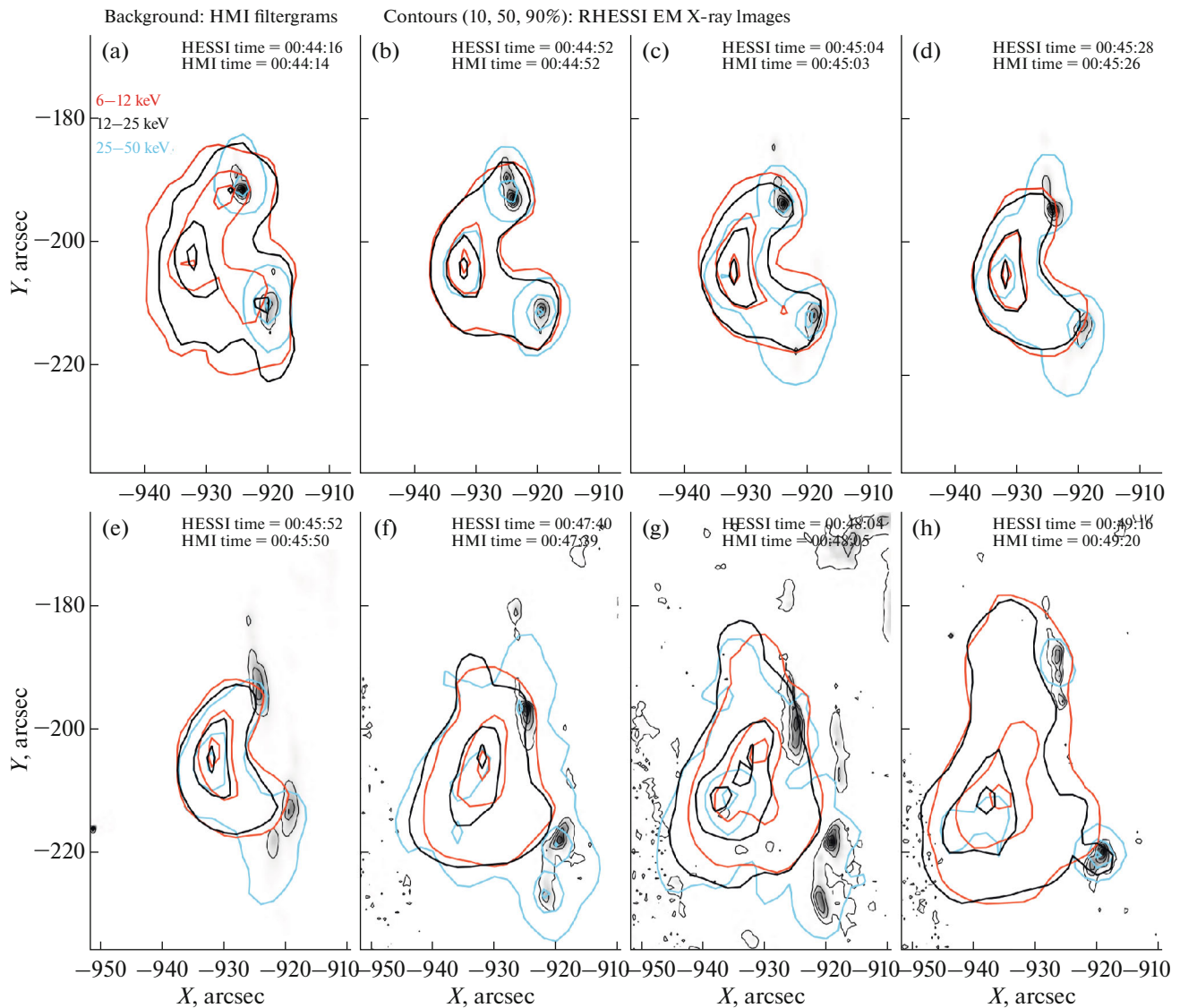


**Fig. 7.** Comparison between the HMI filtergrams (background images and thin black contours) and the RHESSI X-ray sources in the three energy bands of 6–12, 12–25, and 25–50 keV (red, black, and cyan contours, respectively). The contours mark three levels: 10, 50, and 90% from the maximal brightness of the X-ray sources.

4. Using the HMI vector magnetograms we proved that the strongest magnetic field change was associated with the strong magnetic field shear at the PIL. The subsequent long-duration changes of the magnetic field vector was likely connected with the magnetic arcade growth due to the eruption;

5. We also found an apparent expansion of the magnetic field perturbations in the interribbon space. The most interestingly, there was the zipping-like spreading of the magnetic field perturbations. By other words, there was an apparent motion of the magnetic field change region in the direction along the expected PIL possibly co-directional with the displacements of the photospheric and the HXR emission sources;

6. Both stages of the energy release occurred after the onset of accelerated motion (eruption) of the twisted

magnetic structure. The flare loops were under the eruptive structure. The acceleration peak ( $\sim 10 \text{ km s}^{-2}$ ) of the eruptive structure was reached during the first stage of the energy release, and the peak velocity ( $\sim 1700 \text{ km s}^{-1}$ ) was reached approximately during the transition between the first and second stages of the energy release.

To sum up our magnetic field analysis from the methodological point of view we focus an attention on the fact that it was possible to catch the short time interval of the horizontal magnetic field restructuring with an approximate duration of 2 min. It is a few times shorter comparing with the similar values found in the other works (e.g. [36, 39, 40]), and consequently we have more real estimation of the time derivatives of the values composed from LOS magne-

tograms. Only in the statistical work of [39] it was discussed the possibility of the magnetic field change to be as high as  $3 \text{ G s}^{-1}$  (using the SOHO/MDI LOS magnetograms) without a detailed analysis (there could be artifacts), whereas the typical values are in the range of  $0.04\text{--}0.7 \text{ G s}^{-1}$ .

While using LOS magnetograms we should remember that we can interpret this data more-or-less correctly only with the HMI vector magnetograms of worse temporal resolution for particular flare locations on the solar disk. For example, in this work we considered the near-the-limb position and, thus, the horizontal magnetic field is dominant in the LOS data. There is also an additional ad-hoc assumption that the vertical magnetic field component around the PIL is less affected by magnetic field restructuring (however it still requires a statistical proof), and, thus, the major effect of the LOS magnetic field change close to the limb can be only due to the changing horizontal magnetic field. Taking into account an assumption of negligible variations of the vertical magnetic field during the flare, we think that it is possible to make 45-second maps of the horizontal magnetic field component even for on-disk flares.

Along with LOS and vector HMI magnetograms, another key data set in this study are time series of the HMI level 1 filtergrams with high temporal resolution as small as 1.8 s. An inspection of the filtergrams and comparison with the other data used allow us to find interesting peculiarities of the flare energy release dynamics closely related to the magnetic reconnection process:

1. It is shown that the HXR temporal profile is co-temporal with the the photospheric optical emission temporal profile. In other words, each HXR peak has corresponding photospheric emission peak without significant time delays;

2. The double photospheric emission sources found are co-spatial with the double HXR emission sources. In this case, and taking into account the result about the temporal dynamics stated above, we can conclude that precipitating high-energy electrons can be an indirect reason of the photospheric emission (due to energy loss and plasma heating in the low solar atmosphere). HMI filtergrams can be used to trace places of precipitating accelerated electrons with high temporal resolution;

3. The initial photospheric flare impacts were detected in the region of the strongest magnetic field change. Also in this way we separate artifacts and real magnetic measurements;

4. There were two stages of the photospheric emission sources dynamics. During the first one we see the “zipping” motion ( $\sim 25 \text{ km/s}$ ) of two compact emission sources with a characteristic area of  $(1\text{--}2) \times 10^{16} \text{ cm}^2$ . The second stage is characterized by the stabilization of the sources, increasing distance between them, and increasing of their area up to  $10^{17} \text{ cm}^2$ ;

5. The interface between the two stages was co-temporal with the onset of the type III radio bursts. And during the second stage the type II radio burst and growing SXR coronal source has been observed, when the eruptive structure reached its peak velocity.

Here we also want to discuss the usage of the HMI level 1 data from the methodological point of view in the frame of the tasks solved. The photospheric emission sources show regions, where the HMI pipeline algorithm results in non-physical magnetogram pixel values. From our point of view the HMI level 1 data is one of the best ways to verify the standard HMI data products and to separate correct pixels from the distorted one. That’s why we are sure that the observed magnetic field variations (discussed at the beginning of this section) at the PIL seen in the 45-second LOS magnetograms were real measurements in the event studied.

Another advantage of using filtergrams is their high cadence (higher than the other used spatially-resolved data types). Despite of not high photometric capabilities of this data product (due to the line scanning and changing polarization mode) we can study dynamics of the photospheric energy release impacts with great details, that is very important for understanding of magnetic reconnection dynamics. Indeed, from this study we know that the photospheric energy release impacts temporally and spatially correspond to the HXR emission dynamics. Assuming that the photospheric sources correspond to the footpoints of the magnetic loops filled with nonthermal electrons we can analyze indirect manifestations of the magnetic reconnection whose generated electric field is a possible reason for the electrons acceleration. From this point of view the obtained observations are in favour of efficient (we mean reconnection leading to acceleration) magnetic reconnection to be a two-stage process.

It is difficult to say that there was an instant, abrupt transit between the two stages of the flare impulsive phase. Rather, the transition could last for a couple of minutes (see Fig. 6). The main difference between the two stages is connected with the dynamics of the magnetic field and emission sources, which is believed to be a tracer of the magnetic reconnection in the coronal site above the PIL. We are not able here to discuss deep physics of the magnetic reconnection process, but we can state that our observational findings clearly confirm theoretical ideas of the two-stage solar flare scenario [10, 29], where the first stage is a 3D magnetic restructuring and the second one is the so-called the “main” quasi-2D stage within the frames of the “standard model” of eruptive two-ribbon flares. This is the main result of this observational work. Let’s formulate the main peculiarities of these two stages:

1. The first “zipping” stage corresponding to the 3D magnetic reconnection represents the parallel apparent displacement of the compact double footpoint-like photospheric emission sources with an

approximately constant distance between them. These sources correspond to the footpoints of magnetic loops with the strong shear. In this stage, the most intense HXR emission, the maximum acceleration of the eruptive structure, the maximum growth rate of the magnetic flux (the horizontal component of the magnetic field) between two flare ribbons are observed.

2. The second stage is the “main” stage of stabilization of the photospheric sources with their increasing area. Less intense HXR emission (comparing with the first stage) and an increase in the height of the hot flare loops and a further increase in the distance between the double photospheric sources are observed. In this stage, the type III and II radio bursts appear. In this stage we have maximal value of the velocity of the eruptive structure. Most likely, at this stage of the flare impulsive phase, the final formation of the quasi-vertical current sheet under the eruptive magnetic flux rope occurs. The change in the photospheric magnetic field is several times smaller than in the first stage that indicates a smaller value of the electric field in the reconnecting current sheet.

In the end, the following general scenario for this eruptive flare is proposed. Most probably, this flare was initiated due to the tether-cutting magnetic reconnection that was argued in [7]. The tether-cutting reconnection could help to create a twisted flux rope in the active region before the onset of the flare impulsive phase. Then, due to probably the kink [7] or another type of instability the initially twisted flux rope started accelerated upward motion (i.e. eruption). The eruption was likely asymmetric rather than uniform along the flux rope’s axis, similar to what was presented and discussed in [22, 23]. The accompanying 3D “zipping” reconnection could help to loosen the tension of the overlying loops and add the poloidal flux to the erupting flux rope increasing its twist according to [7] and consequently the upward-acting Lorentz force [45]. It reached its maximum around the end of the first “zipping” stage that was evidenced by the peak of the eruptive structure acceleration at that time. Due to this “zipping” reconnection in relatively lower-lying and sheared strong magnetic field electrons were accelerated and produced the sequence of intense bursts of hard X-ray emission, as well as photospheric optical emission. After that, in the second stage of the flare impulsive phase, the major fraction of the energy was released due to the quasi-2D reconnection in the quasi-vertical current sheet higher in the corona (see [32] for the discussion of observations of the current sheet at a later stage of this event).

#### FUNDING

This work is supported by the Russian Science Foundation under grant no. 20-72-10158.

#### OPEN ACCESS

This article is licensed under a Creative Commons Attribution 4.0 International License, which permits use, sharing, adaptation, distribution and reproduction in any medium or format, as long as you give appropriate credit to the original author(s) and the source, provide a link to the Creative Commons license, and indicate if changes were made. The images or other third party material in this article are included in the article’s Creative Commons license, unless indicated otherwise in a credit line to the material. If material is not included in the article’s Creative Commons license and your intended use is not permitted by statutory regulation or exceeds the permitted use, you will need to obtain permission directly from the copyright holder. To view a copy of this license, visit <http://creativecommons.org/licenses/by/4.0/>.

#### REFERENCES

1. Artemyev, A., Zimovets, I.V., Sharykin, I.N., et al., Comparative study of electric currents and energetic particle fluxes in a solar flare and earth magnetospheric substorm, *Astrophys. J.*, 2021, vol. 923, p. 151.
2. Aulanier, G., Janvier, M., and Schmieder, B., The standard flare model in three dimensions. I. strong-to-weak shear transition in post-flare loops, *Astron. Astrophys.*, 2012, vol. 543, p. A110.
3. Aulanier, G., Torok, T., and Demoulin, P., Formation of torus-unstable flux ropes and electric currents in erupting sigmoids, *Astrophys. J.*, 2010, vol. 708, pp. 314–333.
4. Benz, A.O., Flare observations, *Living Reviews in Solar Physics*, 2017, vol. 14, no. 1, p. 2.
5. Berkebile-Stoiser, S., Veronig, A.M., Bein, B.M., et al., Relation between the coronal mass ejection acceleration and the non-thermal flare characteristics, *Astrophys. J.*, 2012, vol. 753, p. 88.
6. Centeno, R., Schou, J., Hayashi, K., et al., The helioseismic and magnetic imager (HMI) vector magnetic field pipeline: Optimization of the spectral line inversion code, *Sol. Phys.*, 2014, vol. 289, pp. 3531–3547.
7. Chen, H., Zhang, J., Cheng, X., et al., Direct observations of tether-cutting reconnection during a major solar event from 2014 February 24 to 25, *Astrophys. J. Lett.*, 2014, vol. 797, p. L15.
8. Cliver, E.W., Solar flare nomenclature, *Sol. Phys.*, 1995, vol. 157, p. 285.
9. Emslie, A.G., Dennis, B.R., Shih, A.Y., et al., Global energetics of thirty-eight large solar eruptive events, *Astrophys. J.*, 2012, vol. 759, p. 71.
10. Fleishman, G.D., Gary, D.E., Chen, B., et al., Decay of the coronal magnetic field can release sufficient energy to power a solar flare, *Science*, 2020, vol. 367, p. 278.
11. Gan, W.Q., Li, Y.P., and Miroshnichenko, L.I., On the motions of RHESSI flare footpoints, *Adv. Space Res.*, 2008, vol. 41, no. 6, pp. 908–913.
12. Halain, J.P., Berghmans, D., Seaton, D.B., et al., The SWAP EUV imaging telescope. Part II: In-flight performance and calibration, *Sol. Phys.*, 2013, vol. 286, no. 1, pp. 67–91.

13. Hirayama, T., Theoretical model of flares and prominences. I: Evaporating flare model, *Sol. Phys.*, 1974, vol. 34, pp. 323–338.
14. Hurford, G.J., Schmahl, E.J., Schwartz, R.A., et al., The RHESSI imaging concept, *Sol. Phys.*, 2002, vol. 210, pp. 61–86.
15. Janvier, M., Aulanier, G., Bommier, V., et al., Electric currents in flare ribbons: Observations and three-dimensional standard model, *Astrophys. J.*, 2014, vol. 788, p. 60.
16. Janvier, M., Aulanier, G., Parlat, E., et al., The standard flare model in three dimensions. III. Slip-running reconnection properties, *Astron. Astrophys.*, 2013, vol. 555, p. A77.
17. Kontar, E.P., Piana, M., and Massone, A.M., Generalized regularization techniques with constraints for the analysis of solar bremsstrahlung X-ray spectra, *Sol. Phys.*, 2004, vol. 225, p. 293.
18. Kuznetsov, S.A., Zimovets, I.V., Morgachev, A.S., et al., Spatio-temporal dynamics of sources of hard x-ray pulsations in solar flares, *Sol. Phys.*, 2016, vol. 291, pp. 3385–3426.
19. Lemen, J.R., Title, A.M., Akin, D.J., et al., The Atmospheric Imaging Assembly (AIA) on the Solar Dynamics Observatory (SDO), *Sol. Phys.*, 2012, vol. 275, pp. 17–40.
20. Lin, R.P., Dennis, B.R., Hurford, G.J., et al., The Reuven Ramaty High-Energy Solar Spectroscopic Imager (RHESSI), *Sol. Phys.*, 2002, vol. 210, pp. 3–32.
21. Liu, C., Deng, N., Lee, J., et al., Evidence for solar tether-cutting magnetic reconnection from coronal field extrapolations, *Astrophys. J. Lett.*, 2013, vol. 788, p. L36.
22. Liu, C., Lee, J., and Jing, J., Motions of hard X-ray sources during an asymmetric eruption, *Astrophys. J. Lett.*, 2010, vol. 721, pp. L193–198.
23. Liu, R., Alexander, D., and Gilbert, H.R., Asymmetric eruptive filaments, *Astrophys. J.*, 2009, vol. 691, pp. 1079–1091.
24. Magara, T., Mineshige, S., and Yokoyama, T., Numerical simulation of magnetic reconnection in eruptive flares, *Astrophys. J.*, 1996, vol. 466, p. 1054.
25. Moore, R.L., Sterling, A.C., Hudson, H.S., et al., Onset of the magnetic explosion in solar flares and coronal mass ejections, *Astrophys. J.*, 2001, vol. 552, pp. 833–848.
26. Pesnell, W.D., Thompson, B.J., and Chamberlin, P.C., The Solar Dynamics Observatory (SDO), *Sol. Phys.*, 2012, vol. 275, pp. 3–15.
27. Petrie, G.J.D., The abrupt changes in the photospheric magnetic and Lorentz force vectors during six major neutral-line flares, *Astrophys. J.*, 2012, vol. 759, no. 1, p. 50.
28. Priest, E.R. and Forbes, T.G., The magnetic nature of solar flares, *Astron. Astrophys. Rev.*, 2002, vol. 10, pp. 313–377.
29. Priest, E.R. and Longcope, D.W., Flux-rope twist in eruptive flares and CMEs: Due to zipper and main-phase reconnection, *Sol. Phys.*, 2017, vol. 292, p. 25.
30. Scherrer, P.H., Schou, J., Bush, R.I., et al., The Helioseismic and Magnetic Imager (HMI) investigation for the Solar Dynamics Observatory (SDO), *Sol. Phys.*, 2012, vol. 275, pp. 207–227.
31. Schmieder, B., Aulanier, G., and Vrsnak, B., Flare-CME models: An observational perspective (invited review), *Sol. Phys.*, 2015, vol. 290, no. 12, pp. 3457–3486.
32. Seaton, D.B., Bartz, A.E., and Darnel, J.M., Observations of the formation, development, and structure of a current sheet in an eruptive solar flare, *Astrophys. J.*, 2017, vol. 835, no. 2, p. 139.
33. Seaton, D.B., Berghmans, D., Nicula, B., et al., The SWAP EUV imaging telescope part I: Instrument overview and pre-flight testing, *Sol. Phys.*, 2013, vol. 286, no. 1, pp. 43–65.
34. Sharykin, I.N. and Kosovichev, A.G., Onset of photospheric impacts and helioseismic waves in X9.3 solar flare of 2017 September 6, *Astrophys. J.*, 2018, vol. 864, no. 1, p. 86.
35. Sharykin, I.N., Kosovichev, A.G., Sadykov, V.M., et al., Investigation of relationship between high-energy X-ray sources and photospheric and helioseismic impacts of X1.8 solar flare of 2012 October 23, *Astrophys. J.*, 2017, vol. 843, p. 67.
36. Sharykin, I.N., Zimovets, I.V., and Myshyakov, I.I., Flare energy release at the magnetic field polarity inversion line during the M1.2 solar flare of 2015 March 15. II. Investigation of photospheric electric current and magnetic field variations using HMI 135 s vector magnetograms, *Astrophys. J.*, 2020, vol. 893, no. 2, p. 159.
37. Sharykin, I.N., Zimovets, I.V., Myshyakov, I.I., et al., Flare energy release at the magnetic field polarity inversion line during the M1.2 solar flare of 2015 March 15. I. Onset of plasma heating and electron acceleration, *Astrophys. J.*, 2018, vol. 864, no. 2, p. 156.
38. Shibata, K. and Magara, T., Solar flares: Magnetohydrodynamic processes, *Living Reviews in Solar Physics*, 2011, vol. 8, p. 6.
39. Sudol, J.J. and Harvey, J.W., Longitudinal magnetic field changes accompanying solar flares, *Astrophys. J.*, 2005, vol. 635, pp. 647–658.
40. Sun, X., Hoeksema, J.T., Liu, Y., et al., Investigating the magnetic imprints of major solar eruptions with SDO/HMI high-cadence vector magnetograms, *Astrophys. J.*, 2017, vol. 839, p. 67.
41. Sun, X., Hoeksema, J.T., Liu, Y., et al., Evolution of magnetic field and energy in a major eruptive active region based on SDO/HMI observation, *Astrophys. J.*, 2012, vol. 748, p. 77.
42. Temmer, M., Veronig, A.M., Kontar, E.P., et al., Combined STEREO/RHESSI study of coronal mass ejection acceleration and particle acceleration in solar flares, *Astrophys. J.*, 2010, vol. 712, no. 2, pp. 1410–1420.
43. Tikhonov, A.N., Regularization of incorrectly posed problems, *Sov. Math. Dokl.*, 1963, vol. 4, no. 6, pp. 1624–1627.
44. Tsuneta, S., Moving plasmoid and formation of the neutral sheet in a solar flare, *Astrophys. J.*, 1997, vol. 483, pp. 507–514.
45. Vrsnak, B., Solar eruptions: The CME–flare relationship, *Astron. Nachr.*, 2016, vol. 337, no. 10, p. 1002.
46. Yang, Y.-H., Cheng, C.Z., Krucker, S., et al., A statistical study of hard X-ray footpoint motions in large solar flares, *Astrophys. J.*, 2009, vol. 693, no. 1, pp. 132–139.
47. Zharkova, V.V., Arzner, K., Benz, A.O., et al., Recent advances in understanding particle acceleration processes in solar flares, *Space Sci. Rev.*, 2011, vol. 159, nos. 1–4, pp. 357–420.